Supplement of Atmos. Chem. Phys., 26, 7165–7191, 2026
https://doi.org/10.5194/acp-26-7165-2026-supplement


Atmospheric Chemistry and Physics
Open Access
EGU

*Supplement of*

# Vertically-resolved source contributions to climate-relevant aerosol properties in Southern Greenlandic fjord systems

**Joanna Alden et al.**

*Correspondence to:* Julia Schmale (julia.schmale@epfl.ch)

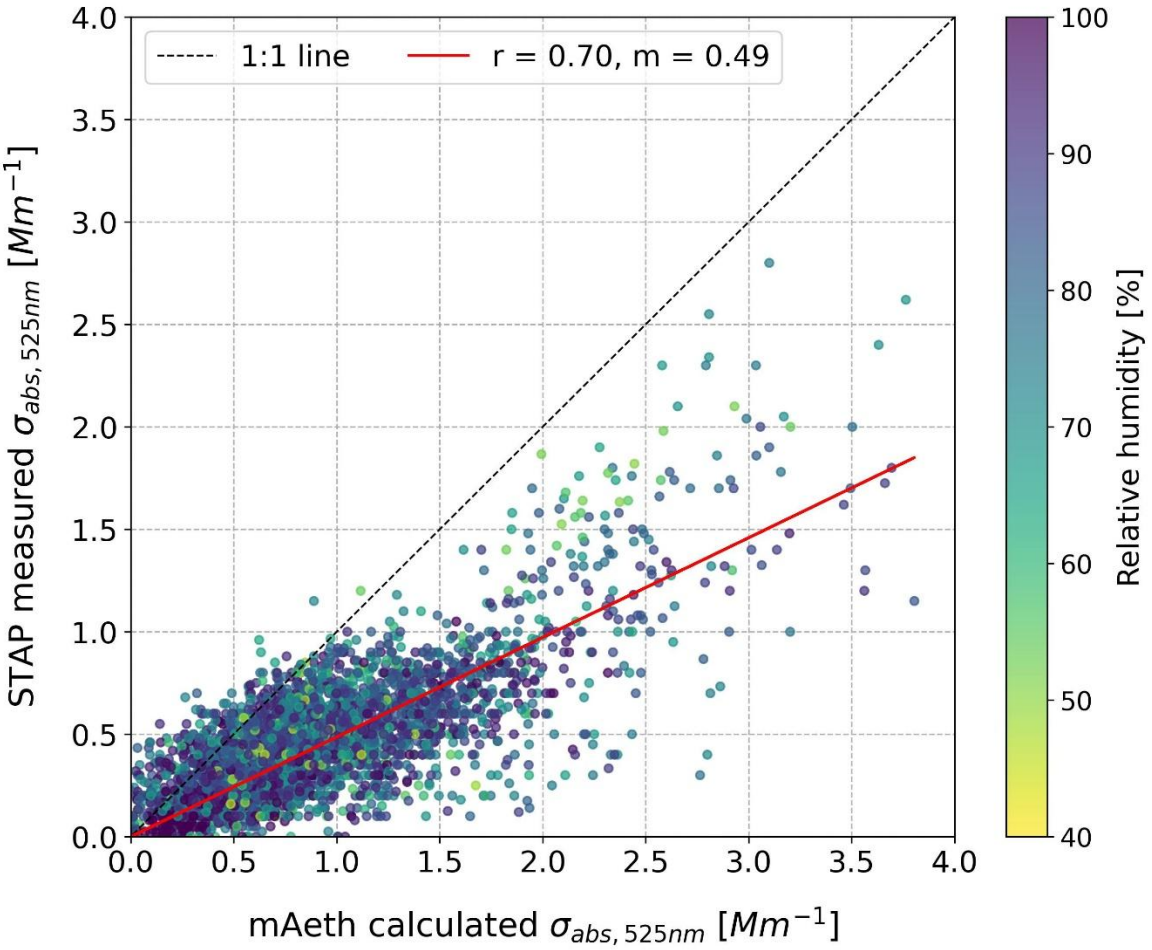


**Figure S1.** Correlation of measured $\sigma_{abs,525}$ by the STAP and the $\sigma_{abs,525}$ calculated from the equivalent black carbon, eBC, mass values given by the mAeth, for background conditions. m is the slope, r the Pearson correlation coefficient. Yellow-purple colour map shows the ambient relative humidity for each measurement. Note this is the outside RH, not the RH after drying in the inlet.

## S1. Comparison of STAP and mAeth

The STAP and mAeth instruments do not provide a 1:1 agreement in absorption measurements due to differences in measurement principles, resolution, and operational constraints. Below is a summary of key differences that explain the discrepancies in absolute absorption coefficient values. Importantly, despite these differences, the temporal variability in absorption coefficients observed between the two instruments are consistent (Pearson r = 0.7).

1. **Measurement principle:** Both instruments are filter-based, but the STAP directly reports absorption coefficients, whereas the mAeth reports equivalent black carbon (eBC) mass. Absorption coefficients from the mAeth are derived using manufacturer-provided mass absorption cross-sections (MAC) from AethLabs. Since MAC values vary considerably in the literature, the calculated absorption is more uncertain and strongly dependent on the chosen MAC.
2. **Detection limits:** The mAeth has a detection limit of ~30 ng $m^{-3}$ (5-min averaging), whereas the STAP achieves ~20 ng $m^{-3}$.
3. **Time resolution:** In low-concentration environments prone to short-lived local spikes, the STAP's higher temporal resolution (1 s vs. 1 min for the mAeth), combined with its lower detection limit, makes it more responsive to rapid changes in absorption.
4. **Operational constraints:** The STAP requires grounding and is highly sensitive to electrical interference and elevated humidity, decreasing the signal to noise ratio, while the mAeth is more robust in these conditions.
5. **Deployment differences:** The mAeth operated continuously throughout the campaign, while the STAP was regularly repositioned to support tethered balloon flights and filter changes, potentially introducing additional variability.

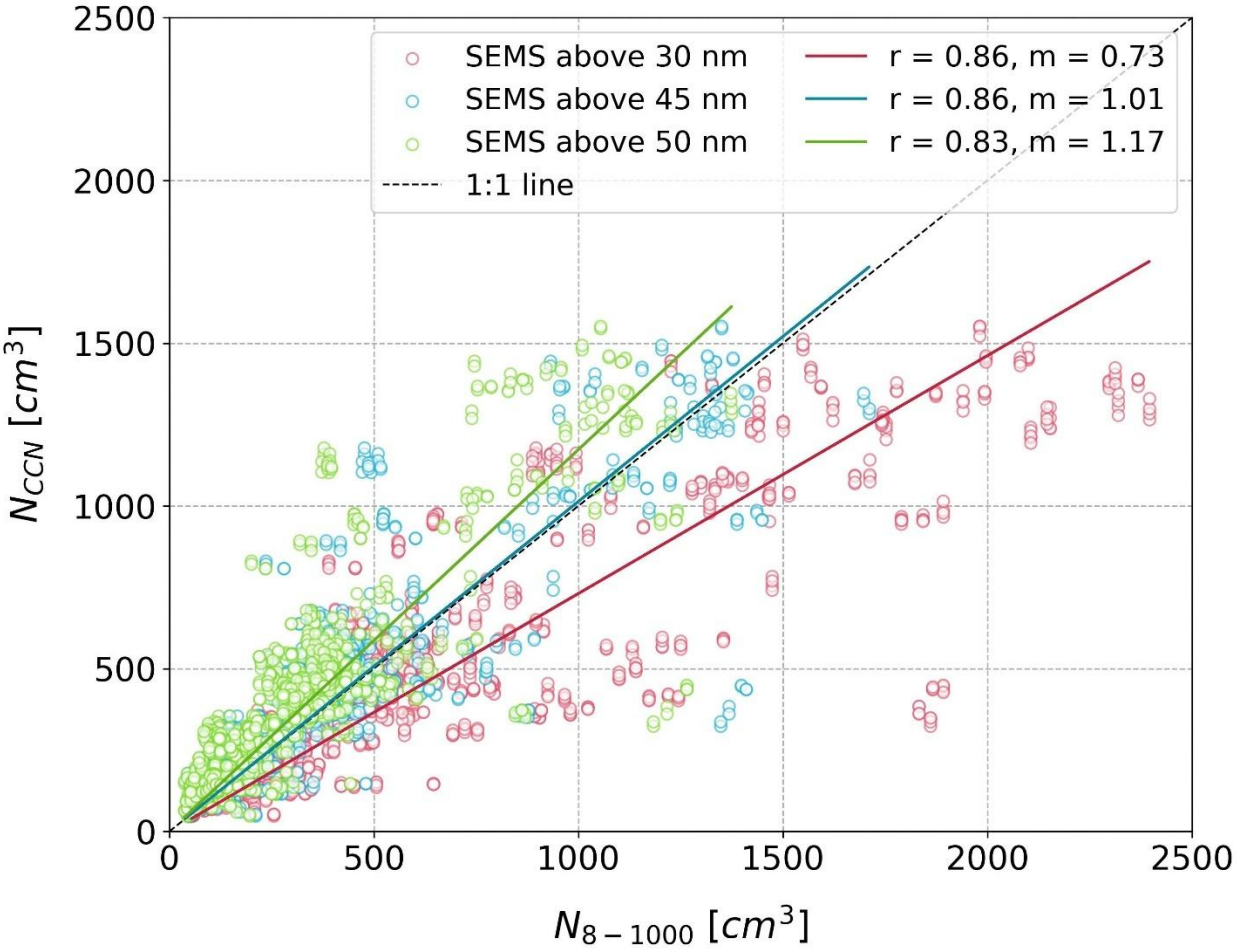


**Figure S2:** Correlation between $N_{CCN}$ at 1% supersaturation ($cm^{-3}$) and Nx-1000 ($cm^{-3}$) where x is the activation diameter cut off of 30 (red circles), 45 (blue circles) or 50 (green circles) nm. Linear regression line and corresponding Pearson's r value and gradient of the slope (m) is given for each activation diameter.

**Table S1: Overview of instruments operated during each flight**. Zero denotes the instrument was not operated, 1 denotes the instrument was present and working, 2 denotes the instrument was present but with only partial acquisition of data due to technical issues.

| Flight | Date | Time | Duration (h) | $CO_2$ | POPS | STAP | mSEMS | Smart Tether | RH/T |
|---|---|---|---|---|---|---|---|---|---|
| 1 | 27.06.2023 | 08:00 | 3.00 | 1 | 1 | 1 | 0 | 1 | 1 |
| 2 | 28.06.2023 | 07:30 | 3.50 | 1 | 1 | 1 | 2 | 1 | 1 |
| 3 | 28.06.2023 | 15:40 | 4.50 | 1 | 1 | 1 | 2 | 1 | 1 |
| 4 | 29.06.2023 | 11:10 | 3.25 | 1 | 1 | 1 | 2 | 1 | 1 |
| 5 | 02.06.2023 | 13:40 | 4.33 | 1 | 1 | 1 | 1 | 1 | 1 |
| 6 | 03.07.2023 | 13:10 | 2.16 | 1 | 1 | 2 | 1 | 1 | 1 |
| 7 | 05.07.2023 | 11:00 | 5.00 | 1 | 1 | 1 | 1 | 1 | 1 |
| 8 | 07.07.2023 | 11:00 | 4.50 | 1 | 1 | 1 | 1 | 1 | 1 |
| 9 | 08.07.2023 | 06:00 | 4.00 | 1 | 1 | 1 | 1 | 1 | 1 |
| 10 | 08.07.2023 | 11:00 | 1.75 | 1 | 1 | 1 | 1 | 1 | 1 |
| 11 | 13.07.2023 | 07:00 | 4.50 | 1 | 1 | 1 | 1 | 1 | 1 |
| 12 | 13.07.2023 | 11:50 | 5.00 | 1 | 1 | 1 | 1 | 1 | 1 |
| 13 | 15.07.2023 | 14:40 | 5.83 | 1 | 0 | 1 | 0 | 1 | 1 |
| 14 | 16.07.2023 | 10:45 | 5.00 | 1 | 1 | 1 | 1 | 1 | 1 |
| 15 | 18.07.2023 | 14:00 | 4.50 | 1 | 1 | 1 | 1 | 1 | 1 |
| 16 | 20.07.2023 | 09:45 | 3.75 | 1 | 1 | 1 | 1 | 1 | 1 |
| 17 | 25.07.2023 | 07:00 | 2.50 | 1 | 1 | 1 | 1 | 1 | 1 |
| 18 | 25.07.2023 | 17:30 | 1.50 | 2 | 1 | 1 | 1 | 2 | 1 |
| 19 | 26.07.2023 | 14:15 | 6.50 | 1 | 1 | 1 | 1 | 1 | 1 |
| 20 | 28.07.2023 | 12:00 | 6.00 | 1 | 1 | 1 | 1 | 1 | 1 |
| 21 | 28.07.2023 | 21:30 | 2.00 | 1 | 1 | 1 | 1 | 1 | 1 |
| 22 | 30.07.2023 | 10:15 | 4.50 | 1 | 1 | 1 | 1 | 1 | 1 |
| 23 | 31.07.2023 | 13:00 | 2.00 | 1 | 1 | 0 | 1 | 1 | 1 |
| 24 | 02.08.2023 | 11:50 | 2.50 | 1 | 1 | 0 | 1 | 0 | 1 |

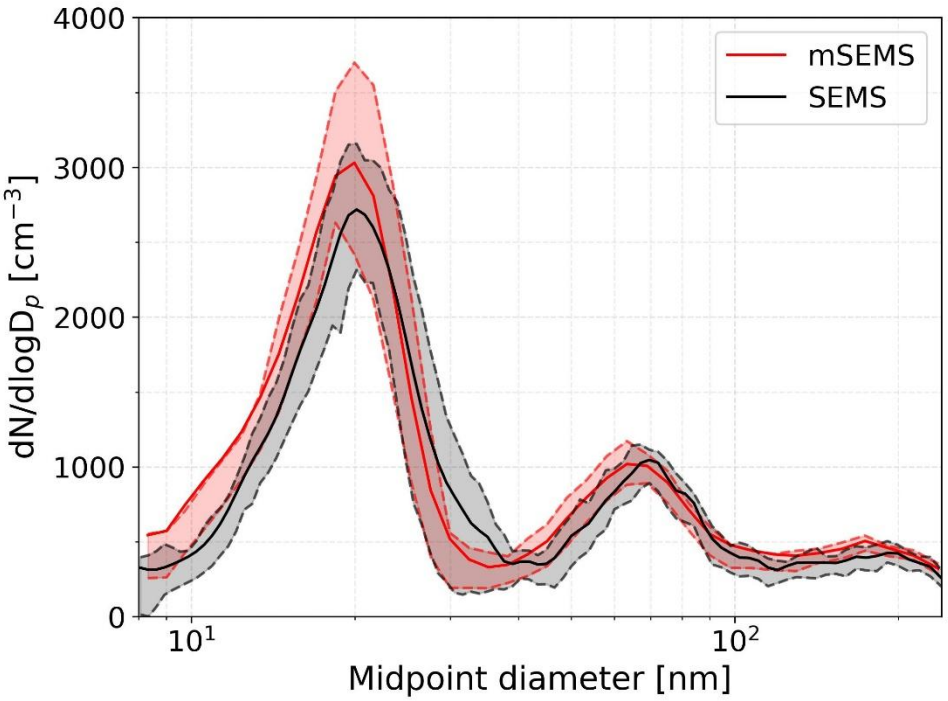


**Figure S3:** Median average and IQR for particle number size distributions (PNSDs) between 8 and 240 nm for mSEMS and SEMS for the period of intercomparison.

40

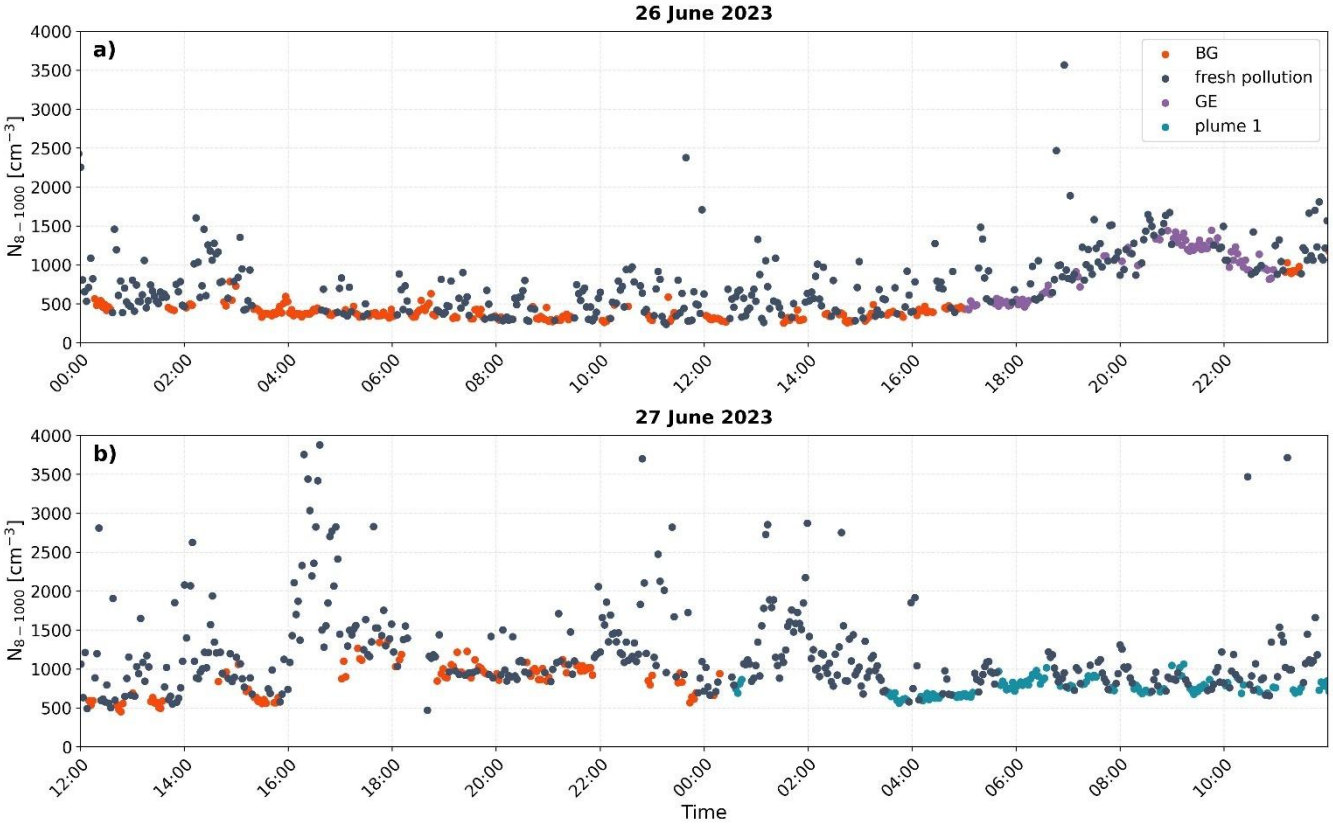


**Figure S4.** Time series of $N_{8\text{-}1000}$ over 24 hour periods for a) the 26th and b) the 27th June 2023 showing the effect of short-lived pollution spikes (navy scatter), growth events (purple scatter) and biomass burning plumes (blue scatter) on the aerosol background (orange scatter).

45

## S2. Within cluster sum of squares and Silhouette score

The Within Cluster Sum of Squares (WCSS) measures the total squared distance between each data point and the centroid of the cluster it is assigned to by a clustering algorithm (Thinsungnoen et al., 2015). The equation for WCSS is as follows:

$$WCSS = \sum_{k=1}^{K} \sum_{x \in C_k} \|x_i - \mu_k\|^2 \quad \text{(S1)}$$

Where $K$ is the total number of clusters, $C_k$ is the set of data points that belong to cluster $k$, $x_i$ is a data point assigned to cluster $k$, $\mu_i$ is the centroid of cluster k and $\|x_i - \mu_k\|^2$ is the squared Euclidean distance between data point $x_i$ and its cluster centroid $\mu_i$.

The smaller the WCSS value, the tighter and more compact the clusters are. Once WCSS is calculated, the *elbow method* can utilised to determine the optimal number of clusters. This method involves plotting the WCSS versus cluster number and looking for the first point where the WCSS values drop off sharply, the "elbow" point. After a certain cluster number, the reduction between increasing cluster numbers will become smaller and the curve will flatten out. The elbow is a semi-subjective point where the rate of decrease of WCSS sharply changes. An example of this method is shown below.

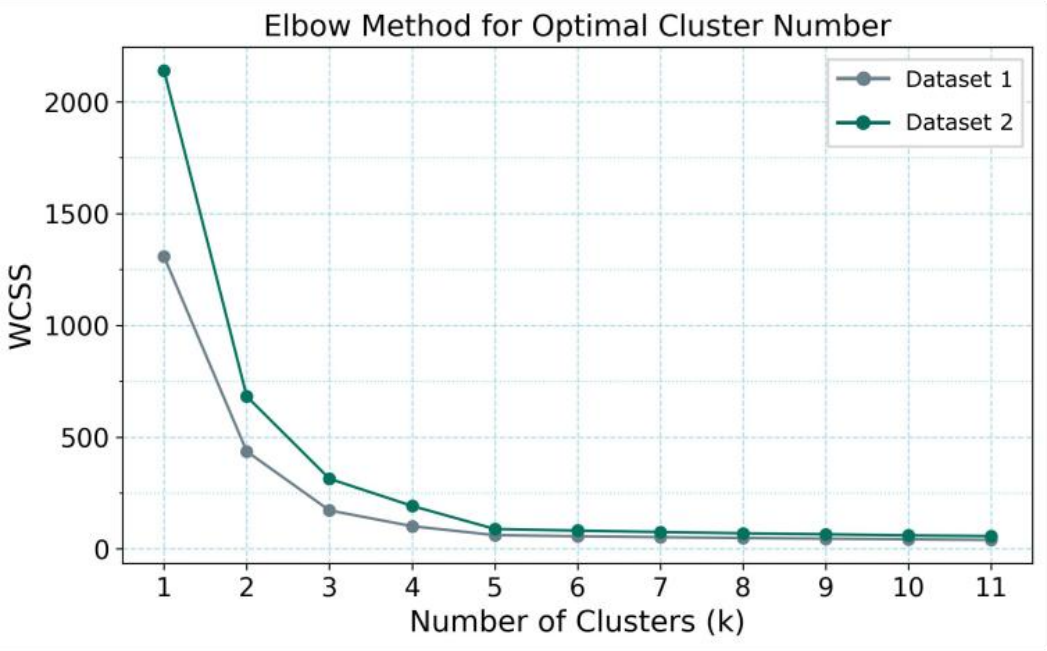


**Figure S5.** Example of Elbow method of determining optimal cluster number using Within Cluster Sum of Squares.

The silhouette score method is another popular method to evaluate the quality of the assigned clusters. However, unlike WCSS which focuses on the compactness of the clusters, the silhouette score considers how well the clusters a separated from each other. For a single data point the equation is as follows:

$$s(i) = \frac{b(i) - a(i)}{\max\left(a(i), b(i)\right)} \tag{S2}$$

Where:

- $a(i)$ is the average distance between the data point $i$ and all other points in the same cluster (measuring cohesion).
- $b(i)$ is the average distance between the data point $i$ and all points in the nearest neighboring cluster (measuring separation).

Silhouette scores range from -1 to +1 with scores closer to +1 indicating that the data point is well-matched to its own cluster and poorly matched to the neighboring cluster. A score or 0 or close to indicates that the data point is on or very close to the decision boundary between two clusters. A negative score indicates that a data point may be assigned to the wrong cluster. A high average silhouette score, therefore, indicates better-defined and well-separated clusters.

**Table S2:** Total number of SEMS scans included in each data category for clustering.

| Source | Total scans (% occurrence in time series) |
|---|---|
| BG | 5463 (33.5%) |
| Pollution | 8215 (50.4%) |
| GE | 1308 (8.0%) |
| P1 | 460 (2.8%) |
| P2 | 739 (4.5%) |
| P3 | 108 (0.7%) |

Note: periods of precipitation have been removed from the data prior to clustering due to wet deposition removing aerosols from atmosphere.

80

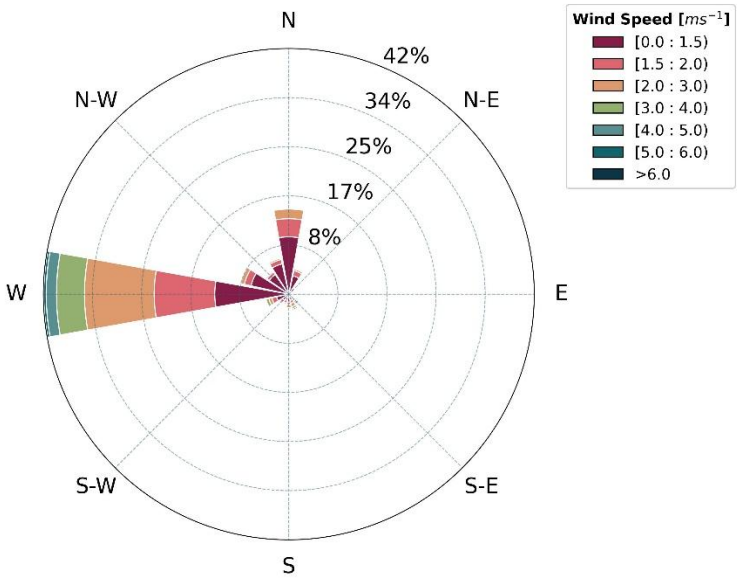


**Figure S6:** Windrose showing frequency, direction (°) and speed (m $s^{-1}$) on the ground for the entire campaign**.**

**Table S3:** Percentage occurrence of each defined range of wind directions throughout the entire campaign period.

| Defined wind direction category | Wind direction (°) | % occurrence |
|---|---|---|
| W | 247.5 – 292.5 | 51 |
| NW | 292.5 – 337.5 | 10.2 |
| N | 337.5 – 22.5 | 21.5 |
| NE | 22.5 – 67.5 | 3.2 |
| E | 67.5 – 112.5 | 1.2 |
| SE | 112.5 – 157.5 | 4.2 |
| S | 157.5 – 202.5 | 4.6 |
| SW | 202.5 – 247.5 | 4.5 |

85

**Table S4.** Summary of precipitation periods throughout campaign. Start and end times of fog on the ground was determined using ceilometer β measurements.

| Event type | Start | End | Fog on Ground Start | Fog on Ground End |
|---|---|---|---|---|
| Rain | 21/06/2023 10:00 | 21/06/2023 24:00 | - | - |
| Fog | 22/06/2023 00:00 | 22/06/2023 17:00 | - | - |
| Rain | 23/06/2023 03:00 | 23/06/2023 04:00 | - | - |
| Fog | 23/06/2023 22:00 | 24/06/2023 09:30 | - | - |
| Fog | 24/06/2023 21:00 | 25/06/2023 12:00 | - | - |
| Fog | 25/06/2023 21:00 | 26/06/2023 11:00 | - | - |
| Fog | 08/07/2023 00:00 | 08/07/2023 09:00 | - | - |
| Fog | 13/07/2023 04:15 | 13/07/2023 16:00 | 13/07/2023 06:00 | 13/07/2023 08:30 |
| Rain | 16/07/2023 05:30 | 16/07/2023 09:00 | - | - |
| Rain | 17/07/2023 02:15 | 17/07/2023 08:00 | - | - |
| Fog | 18/07/2023 07:00 | 18/07/2023 10:00 | - | - |
| Rain | 18/07/2023 19:00 | 19/07/2023 18:00 | - | - |
| Fog | 19/07/2023 19:00 | 20/07/2023 17:00 | 19/07/2023 19:00 | 20/07/2023 17:00 |
| Rain | 20/07/2023 17:00 | 21/07/2023 08:00 | - | - |
| Fog | 24/07/2023 23:00 | 26/07/2023 12:00 | 25/07/2023 00:00 | 25/07/2023 06:00 |
| Fog | 31/07/2023 00:00 | 31/07/2023 11:00 | 31/07/2023 00:00 | 31/07/2023 09:30 |

**Table S5.** Ground-based Cluster classification of PNSDs and their relative abundance. The distribution of clustered PNSDs from a total of 16,293 total PNSDs.

| Cluster name | Number of PNSDs per cluster | % of total clustered PNSDs (Total = 16,293) |
|---|---|---|
| *Pollution* $c_1$ | 2396 | 14.7 |
| *Pollution* $c_2$ | 3206 | 19.7 |
| *Pollution* $c_3$ | 2613 | 16.0 |
| *BG* $c_1$ | 1652 | 10.1 |
| *BG* $c_2$ | 2113 | 13 |
| *BG* $c_3$ | 1698 | 10.4 |
| *GE* $c_1$ | 284 | 1.7 |
| *GE* $c_2$ | 450 | 2.8 |
| *GE* $c_3$ | 574 | 3.5 |
| *P1* $c_1$ | 108 | 0.7 |
| *P1* $c_2$ | 86 | 0.5 |
| *P1* $c_3$ | 219 | 1.3 |
| *P1* $c_4$ | 47 | 0.3 |
| *P2* $c_1$ | 282 | 1.7 |
| *P2* $c_2$ | 161 | 1.0 |
| *P2* $c_3$ | 75 | 0.5 |
| *P2* $c_4$ | 221 | 1.4 |
| *P3* $c_1$ | 36 | 0.2 |
| *P3* $c_2$ | 29 | 0.2 |
| *P3* $c_3$ | 43 | 0.3 |

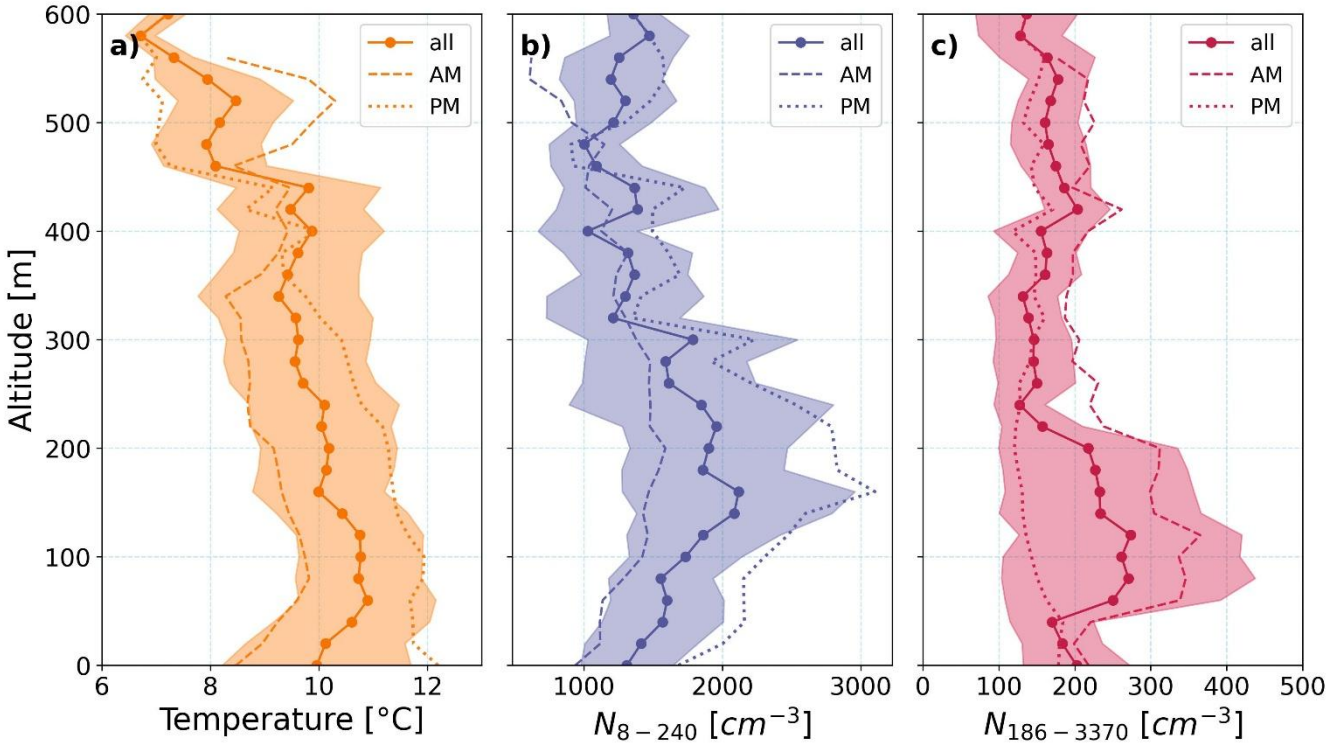


**Figure S7.** Vertical profile of a) temperature (orange), b) total number concentration between 8-240 nm ($N_{8\text{-}240}$, purple) and, c) total number concentration between 186-3370 nm ($N_{186\text{-}3370}$, crimson) averaged over all BG flights. Shaded regions show IQR, solid line and markers show median for all flights, while dashed and dotted lines show mean for morning (between 07:00-13:00) and afternoon flights (between 13:00-19:00) respectively. Profiles are spatially averaged to 20 m. All aerosol vertical measurements have been corrected for standard temperature and pressure.

## S3. Classification Algorithm for clustered CL61 measurements

Based on previous long-term measurements from the group, a classification algorithm was developed in hand with manufacturer guidelines and literature data (Soldati, 2024). The algorithm relies on the fact that measured properties of aerosols, hydrometeors and cloud particles change based on their chemical composition, size, shape and phase and that specific thresholds for both the attenuated backscatter (β) and the linear depolarisation ratio (LDR) can be set to distinguish between classes.

To identify and distinguish these patterns in β and LDR data associated with different atmospheric conditions in a more systematic way, we applied an unsupervised clustering approach using the K-means algorithm. The choice of cluster number was overestimated to ensure all subtle atmospheric features were captured fully. Satisfactory results were obtained with as few as 8 clusters over a 24-hour period, but higher N can, in theory, be used to capture more refined atmospheric structures. To improve clustering, range (altitude) was added as a third feature, allowing discrimination between near-surface and elevated features. Prior to clustering, each feature was standardized (zero mean, unit variance), with the range component scaled down by 75% to reduce its influence on the clustering outcome. A rule-based classification was then defined which relied on hard thresholds in β and LDR to distinguish between clear air, aerosols, clouds, and precipitation. Thresholds were defined based on a combination of direct ceilometer observations and existing literature (Ansmann et al., 2010; Burton et al., 2015; Groß et al., 2012, 2013; Haarig et al., 2018). For particle shape information, LDR was used, with reference values adapted from the Vaisala CL61 instrument guide. Table S6 summarises the thresholds for β.

**Table S6:** Summary of proposed cut-off thresholds for attenuated backscatter, β**:**

| **Atmospheric class** | **Min – Max β ($m^{-1}$ $sr^{-1}$)** |
|---|---|
| Clear atmosphere | $<1\times10^{-6}$ |
| Aerosol | $1\times10^{-6} – 5\times10^{-6}$ |
| Mid-density (rain/snow) | $5\times10^{-6} – 5\times10^{-5}$ |
| High-density (clouds) | $>5\times10^{-5}$ |

From approximate ranges for typical LDR values as given by Vaisala in their white paper on depolarisation measurements with the ceilometer, the following classes and associated LDR ranges were defined (Soldati, 2024):

**Table S7:** Summary of proposed classes and their respective linear depolarisation ratio, LDR, ranges.

| **Aerosol class (i.e. $\beta < 5\times10^{-6}$)** | **LDR range** | **Hydrometeor class (i.e. $\beta > 5\times10^{-6}$)** |
|---|---|---|

| | | |
|---|---|---|
| Smoke/Pollution/Marine | 0 – 0.1 | Liquid droplets |
| Marine-Smoke-Dust mix | 0.1 – 0.2 | Mixed phase |
| Desert dust | 0.2 – 0.3 | Snow |
| Aerosol-like solid particles (i.e. Volcanic ash) | 0.3 – 0.4 | Ice crystals |
| Aerosol-like highly depolarising particles | 0.4 – 0.5 | |
| | 0.5 – 1.0 | Graupel |

Finally, classification could then be in one of two ways:

**Element-wise**: Assigning a category to each individual (β, LDR) observation pair, by independent classification of each pair (β(r,t), LDR(r,t)) at a each time and range.

**Cluster-wise**: Classification of the entire cluster based on the clusters average β and LDR

The "Smoke/Pollution/Marine" category occurs mainly within the lowest 500 m (Fig. S8). There is a diurnal cycle, with increased frequency of occurrence beginning around 09:00LT, with a gradual rise in the height of the affected layer over the day. This pattern likely reflects the daytime boundary layer growth driven by surface heating and co-varies with observations of aerosols on the ground and in the vertical (Fig. S7).

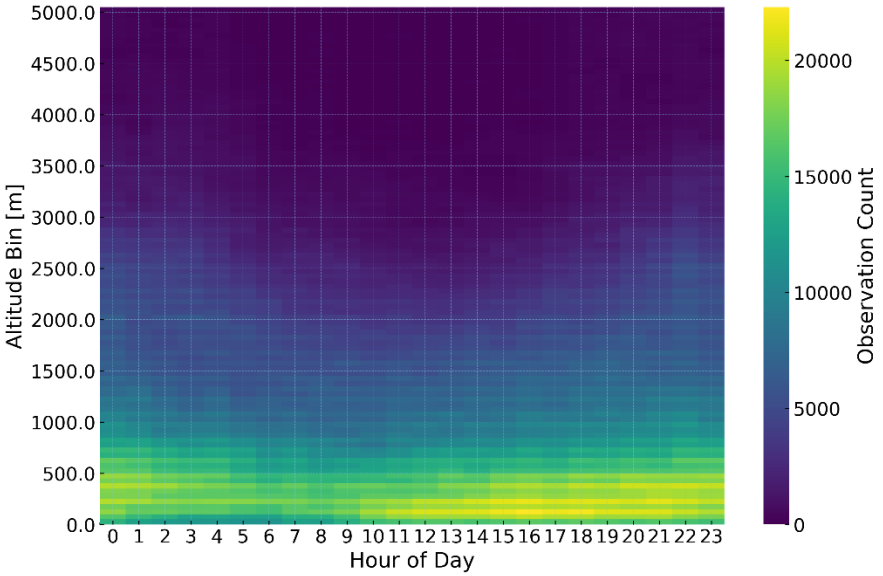


**Figure S8.** Diurnal variation of counts for the "Smoke/Pollution/Marine" category of ceilometer data for the entire campaign binned in 50 m altitude intervals. Biomass burning plume periods have been removed.

## S4. NPF parameters

Table S8 gives a summary of particle growth events. The growth rate (GR) is the rate at which the diameter, $D_p$, changes with time, and is described by the following equation:

$$GR = \frac{\Delta D_p}{\Delta t} = \frac{D_{p2} - D_{p1}}{t_2 - t_1} \quad \text{(S3)}$$

where $D_{p1}$ and $D_{p2}$ are the particle diameters at $t_1$ and $t_2$ respectively.

The condensation sink (CS) is the rate at which a molecule in the vapour phase collides with the surface of a pre-existing particle effectively taking the molecule out of the vapour phase. It is calculated from the aerosol particle number size distribution (Kulmala et al., 2012):

$$CS = 4\pi D \sum_{D_p} d_{D_p} \beta_{m,D_p} N_{D_p} \quad \text{(S4)}$$

Where $D$ is the diffusion coefficient of the diffusing vapour, $\beta_{m,D_p}$ is the transition regime correction as in (Kulmala et al., 2012) and $N_{D_p}$ is the particle number at diameter $D_p$.

The coagulation sink is the rate at which a molecule is removed via coagulation and can be determined from the below equation given by Lehtinen et al., 2007 to simplify calculation of the coagulation sink from the condensation sink:

$$CoagS = CS\left(\frac{D_p}{0.71}\right)^{-1.6} \quad \text{(S5)}$$

**Table S8:** Summary table of particle growth events with relevant variables given as an average during the growth event period. Growth events periods are defined as the 6 hours following the first measurement of a nucleation mode peak. [a]GR : calculated growth rate between 8 and 25 nm. [b]CS: calculated condensation sink [c]CoagS: calculated coagulation sink. [d]Distance: estimated distance of newly grown particles from source of nucleation. [e]SR: downward solar radiation. [f]T: air temperature. [g]WS: wind speed. [h]RH: relative humidity.

| Start Datetime | End Datetime | GR[a] [nm hr$^{-1}$] | CS[b] [s$^{-1}$] | CoagS[c] [s$^{-1}$] | Distance[d] [km] | $N_{191\text{-}9300}$ [cm$^{-3}$] | SR[e] [W m$^{-2}$] | T[f] [°C] | WS[g] [m s$^{-1}$] | RH[h] [%] |
|---|---|---|---|---|---|---|---|---|---|---|
| 23/06/2023 10:08:00 | 23/06/2023 16:08:00 | 4.1 | 9.1E-04 | 1.9E-05 | 15.5 | 8.26 | 595.6 | 10.0 | 2.9 | 75.9 |
| 24/06/2023 12:04:00 | 24/06/2023 18:04:00 | 3.0 | 1.1E-03 | 2.3E-05 | 22.9 | 35.7 | 658.6 | 11.1 | 3.2 | 70.2 |
| 25/06/2023 11:35:00 | 25/06/2023 17:35:00 | 7.6 | 1.8E-03 | 3.0E-05 | 5.9 | 33.1 | 660.2 | 12.1 | 2.1 | 66.6 |
| 26/06/2023 14:03:00 | 26/06/2023 20:03:00 | 3.2 | 1.2E-03 | 2.1E-05 | 13.0 | 47.4 | 335.8 | 10.8 | 1.9 | 73.4 |
| 30/06/2023 11:04:00 | 30/06/2023 17:04:00 | 1.7 | 3.6E-04 | 9.5E-06 | 31.8 | 6.33 | 700.6 | 12.9 | 2.5 | 47.7 |
| 01/07/2023 10:21:00 | 01/07/2023 16:21:00 | 2.7 | 7.2E-04 | 1.9E-05 | 18.1 | 14.9 | 656.4 | 11.3 | 2.3 | 51.5 |
| 05/07/2023 12:03:00 | 05/07/2023 18:03:00 | 2.6 | 1.8E-03 | 3.4E-05 | 19.7 | 61.7 | 580.2 | 14.5 | 2.4 | 66.3 |
| 07/07/2023 11:31:00 | 07/07/2023 17:31:00 | 5.6 | 2.2E-03 | 4.3E-05 | 8.1 | 66.9 | 538.7 | 13.0 | 2.1 | 73.7 |
| 08/07/2023 08:28:00 | 08/07/2023 14:28:00 | 6.9 | 1.9E-03 | 3.1E-05 | 5.5 | 79.8 | 566.6 | 10.8 | 1.8 | 81.5 |
| 09/07/2023 09:21:00 | 09/07/2023 15:21:00 | 3.7 | 2.0E-03 | 3.4E-05 | 8.9 | 95.3 | 469.9 | 14.1 | 1.5 | 69.6 |
| 10/07/2023 14:11:00 | 10/07/2023 20:11:00 | 2.6 | 2.3E-03 | 4.0E-05 | 13.5 | 120.0 | 351.6 | 19.2 | 1.6 | 60.3 |
| 11/07/2023 11:40:00 | 11/07/2023 17:40:00 | 3.6 | 2.3E-03 | 3.8E-05 | 12.1 | 141.0 | 439.7 | 16.9 | 2.0 | 71.3 |
| 16/07/2023 15:24:00 | 16/07/2023 21:24:00 | 1.9 | 2.0E-03 | 2.8E-05 | 24.2 | 31.5 | 319.0 | 11.9 | 2.1 | 79.9 |
| 26/07/2023 14:03:00 | 26/07/2023 20:03:00 | 1.5 | 8.3E-04 | 2.4E-05 | 30.7 | 64.3 | 380.9 | 13.3 | 1.7 | 73.3 |
| 28/07/2023 12:28:00 | 28/07/2023 18:28:00 | 5.2 | 1.8E-03 | 3.1E-05 | 7.0 | 43.6 | 577.2 | 11.5 | 3.2 | 76.4 |
| 30/07/2023 10:30:00 | 30/07/2023 16:30:00 | 5.5 | 1.0E-03 | 2.6E-05 | 12.5 | 32.9 | 513.1 | 9.4 | 3.1 | 83.7 |
| 31/07/2023 12:29:00 | 31/07/2023 18:29:00 | 4.1 | 9.1E-04 | 1.9E-05 | 15.5 | 8.26 | 595.6 | 9.96 | 2.9 | 75.9 |

## S5. Estimation of distance travelled from nucleation location

To estimate the horizontal distance that newly formed particles may travel during growth from their nucleation site to the measurement location, we apply the following simplified approach:

$$Distance\ travelled\ = \frac{\Delta D_p}{GR_{8-25}} \times \mathrm{WS} \quad \text{(S6)}$$

where $\Delta D_p$ is the difference in particle size in m between nucleation diameter and first measurable diameter by SEMS, taken as from 2 to 8 nm; $GR_{8\text{-}25}$ is the particle growth rate (m $s^{-1}$) between 8 and 25 nm and WS is the ambient wind speed measured (m $s^{-1}$).

Growth rates were derived from the observed size evolution in the 8–25 nm size range, calculated using the log-normal distribution method outline in Kulmala et al., 2012.To estimate the full transport distance from the earliest stage of particle formation, we assume that the calculated growth rate between 8 and 25 nm is representative of growth across a broader range, and apply it from 2 to 25 nm. This assumption allows for a first-order approximation of the particle residence time in the growth phase and hence their horizontal transport distance. Wind speed (WS) values per event were defined as the windspeed measured when nucleation mode was first observed per event by SEMS at NIRS. Estimated distances newly formed particles travelled from nucleation site per growth event measured at NIRS are shown in Figure S9 for 8 events chosen to display the full variation in distances from closest to furthest from Narsaq.

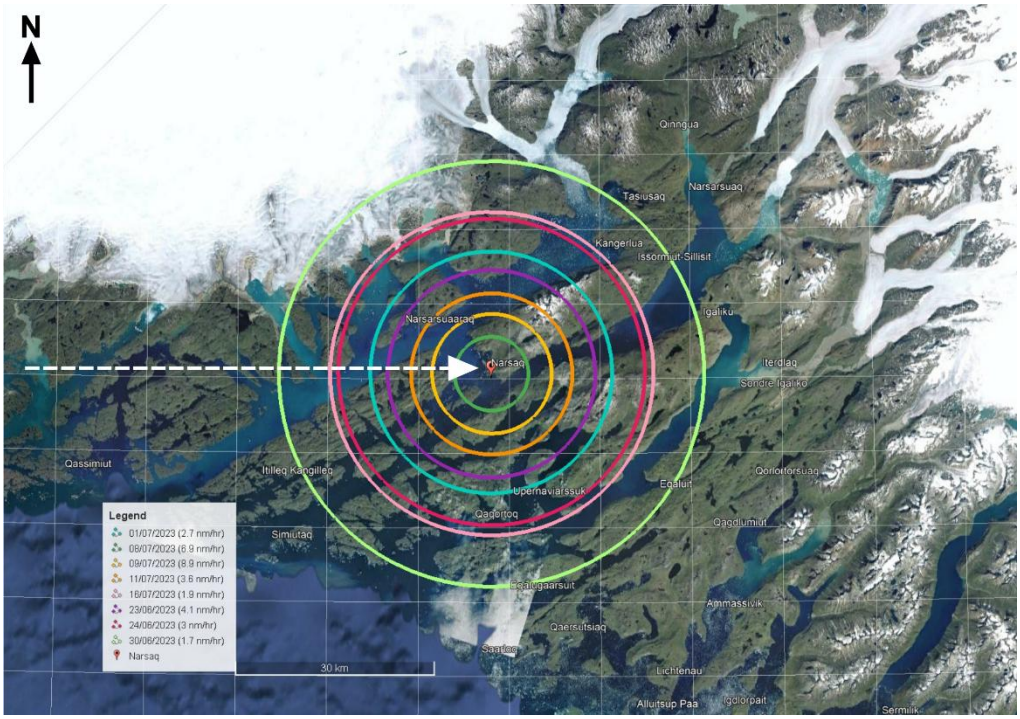


**Figure S9:** Map of the region surrounding Narsaq with a range of estimated distances travelled from nucleation site for 8 growth events overlaid as coloured circles. Prevailing wind direction shown with dashed white arrow. Maps data: © Google Earth Pro (v7.3.6.10201) 2025; images © Landsat/Copernicus and U.S. Geological Survey, Narsaq, 60°58’12.37” N 46°02’37.84”, elevation 0 m.

175

## S6. Inversion detection methodology

Temperature inversions were identified using a simple custom algorithm designed to analyse vertical profiles of atmospheric temperature with altitude. This method builds on the observations and principles from (Fochesatto, 2015; Mayfield and Fochesatto, 2013) to be adapted for higher-resolution vertical flight data and is described in full in (Pohorsky et al., 2025).The key steps included:

1. **Data processing:**
    - Temperature profiles were first smoothed with a gaussian filter to reduce noise while preserving the inflection points.
2. **Gradient calculation:**
    - Vertical temperature gradient (dT/dz) was computed using central differencing. Inversions were flagged when dT/dz exceeded a user defined threshold, usually taken as 0.2°C per 100 m.
    - Gradient values varied between ~0.3 – 3.1 °C per 100 m.
3. **Layer detection and validation**
    - To distinguish discrete layers, we required inversions to meet two criteria:
        i. A minimum thickness, defined by the user and usually 40 – 50 m, to reduce false positives from small fluctuations.
        ii. A minimum vertical separation between adjacent inversions, also user defined, to ensure physical significance.
    - This approach parallels Pohorsky et al., 2025, with a simplified scheme prioritising gradient threshold for computational efficiency.
    - Similar to Pohorsky et al., 2025, we validated thresholds per flight through visual comparison of the gaussian smoothed data, and the unsmoothed data, and knowledge of the system. However, for this work, thresholds were varied slightly between flights to accommodate the large range of processes and complicated boundary layer conditions captured during the campaign, from biomass burning plumes to ground particle growth events.
    - Detected inversions could then be simply classified into “surface-based inversions” or “elevated inversions”.

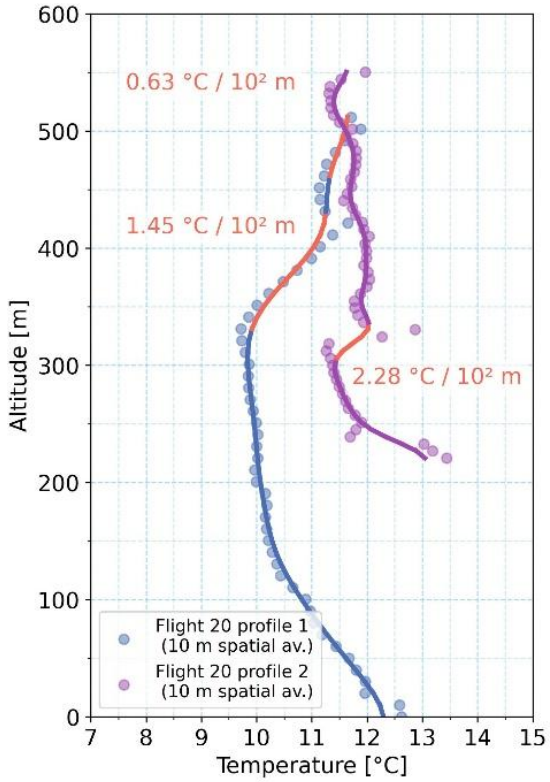


**Figure S10:** Temperature profiles taken using the helikite between 12:05-18:00LT on the 28th July,2023. Temperature inversions are indicated in orange. Profile 1 is the ascent flight of the helikite starting at 12:05 while profile two is the descent flight back to the surface.

205

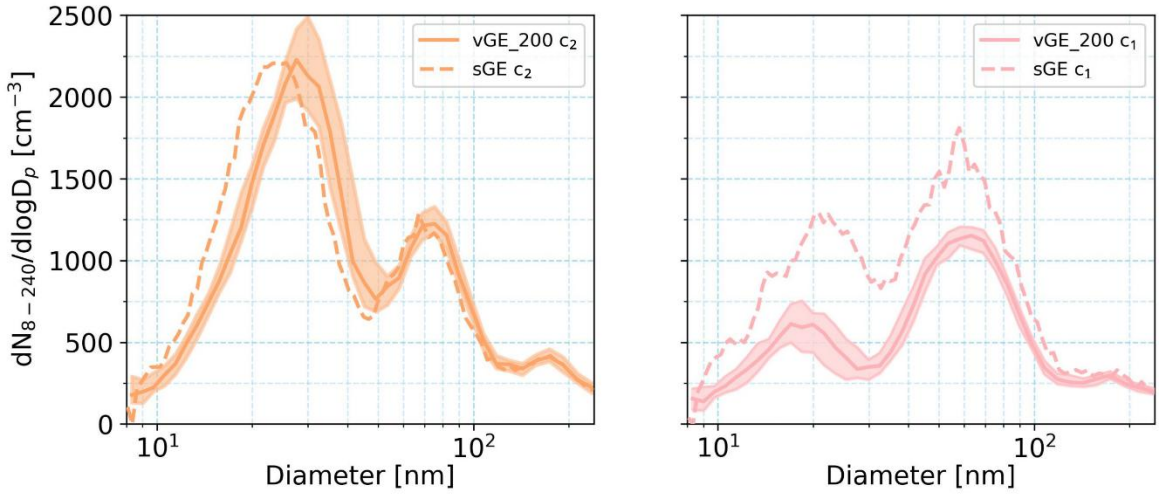


**Figure S11.** Comparison of clustered PNSDs on the ground (dashed line) versus between 200-300 m altitude (median and IQR).

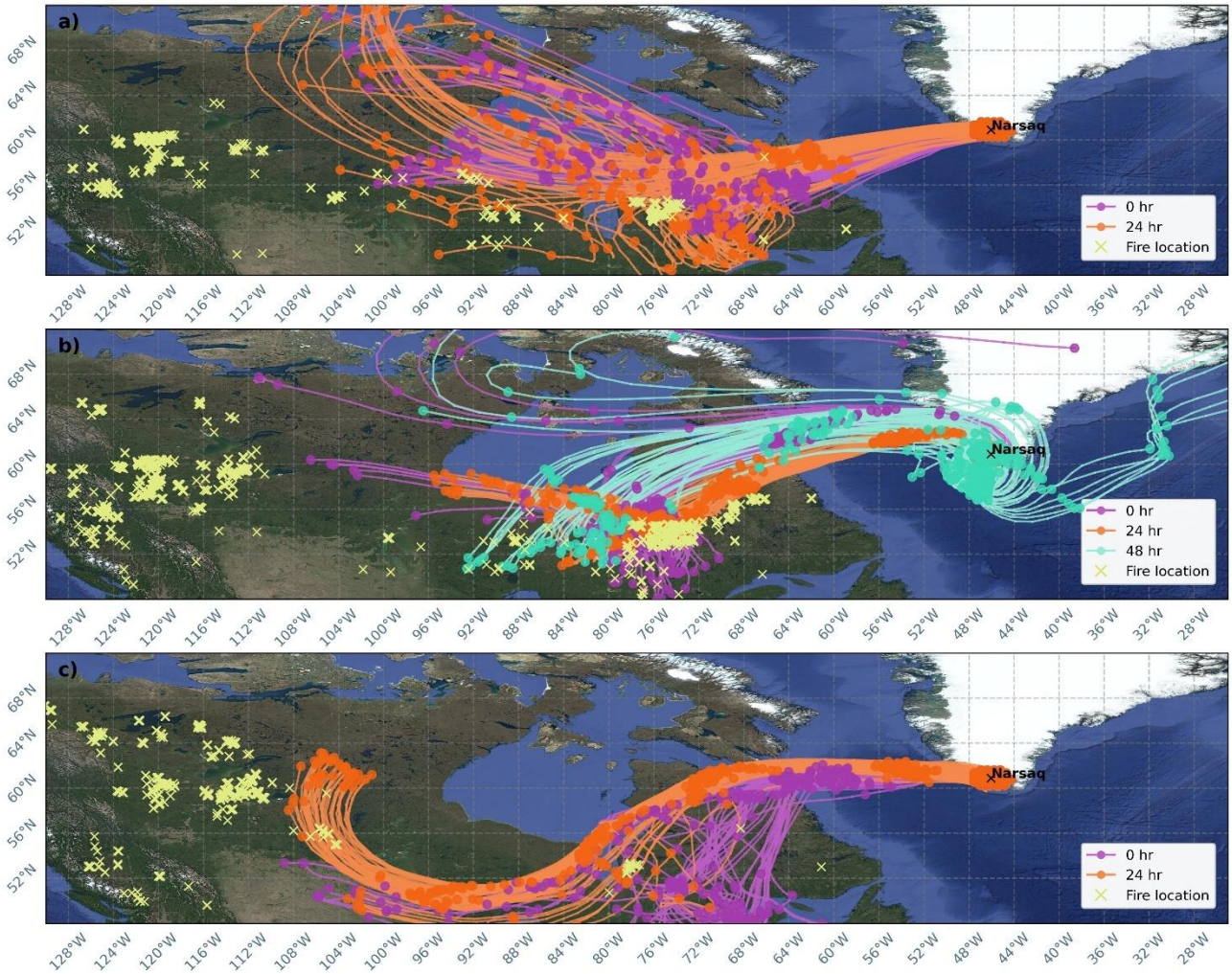


**Figure S12.** Lagranto back-trajectories calculated for 120 hours before a) plume 1, b) plume 2 and c) plume 3, using ERA5 re-analysis data, with a starting atmospheric pressure range of 750 – 650 hPa based on ceilometer observations. Circle markers along the trajectories correspond to 24 hour periods of the 120 hour run time. Trajectories were calculated backwards from the observational start of each plume in Narsaq (purple), for 24 hours after (orange) and 48 hours after (turquoise) if applicable. Fire locations (yellow x) are taken from the Moderate Resolution Imaging Spectrometer (MODIS) and Visible Infrared Imaging Radiometer Suite (VIIRS) data on the Fire information and Resource Management System (FIRMS) archive. Maps data: © Google Earth Pro (v7.3.6.10201) 2025; images © Landsat/Copernicus and U.S. Geological Survey, Data SIO, NOAA, U.S. Navy, NGA, GEBCO.

210

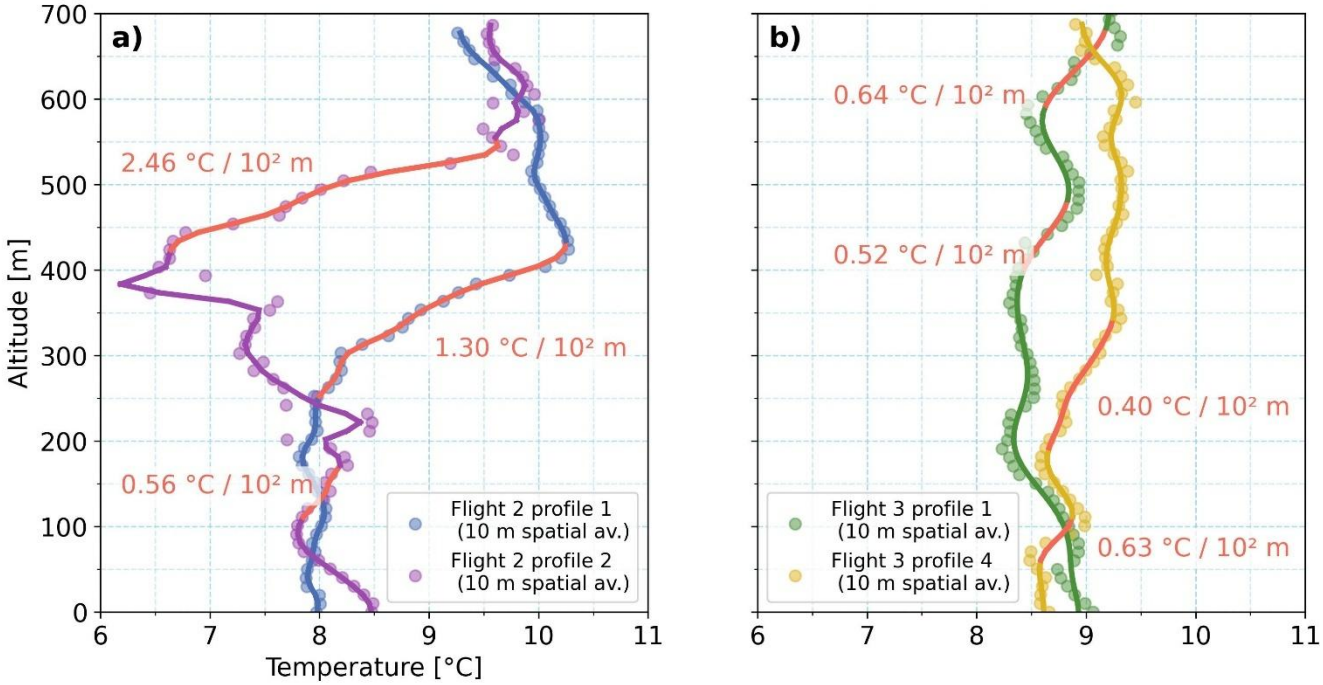


**Figure S13:** Temperature profiles taken using the helikite between 07:39-11:22LT and 16:08-20:52LT on the 28th June, 2023. Temperature inversions are indicated in orange.

## S7. Plume 2

We now examine *plume 2*, to investigate how its different transport history and vertical structure affected aerosol properties at the ground and in the lower atmosphere. Figure S14a-d shows the clustered PNSDs for the period of *plume 2* based on SEMS ground measurements. As with *plume 1*, 4 bi-modal clusters were found to describe this plume on the ground; 1) *P2 c*$_1$, peaking at 39 and 87 nm; 2) *P2 c*$_2$, dominated by a peak at 28 nm with Aitken mode at 100 nm and associated with a growth event; 3) *P2 c*$_3$, with a peak in the Aitken mode at 80 nm and a peak in the accumulation mode above 240 nm; and 4) *P2 c*$_4$, with peaks at 23 nm and 75 nm. All clusters show a clear shift in Aitken mode diameter to higher values compared to the background clusters, and a progressive and distinct increase in accumulation mode concentration as the plume period progresses. Figure S14e shows the time series of $N_{8\text{-}1000}$ with the occurrence of each cluster shaded. Clusters with dominant small Aitken modes (likely originating from growth events) are only observed during daytime hours, while *P2 c*$_4$ dominates overnight, likely representing residual background or aged plume influence. While *P2 c*$_4$ resembles *BG c*$_2$, it is distinguished by an Aitkin mode 9 nm larger in diameter and additional shoulders in the PNSD at 23 and 60 nm, indicating possible broadening due to an influx of new ultrafine particles.

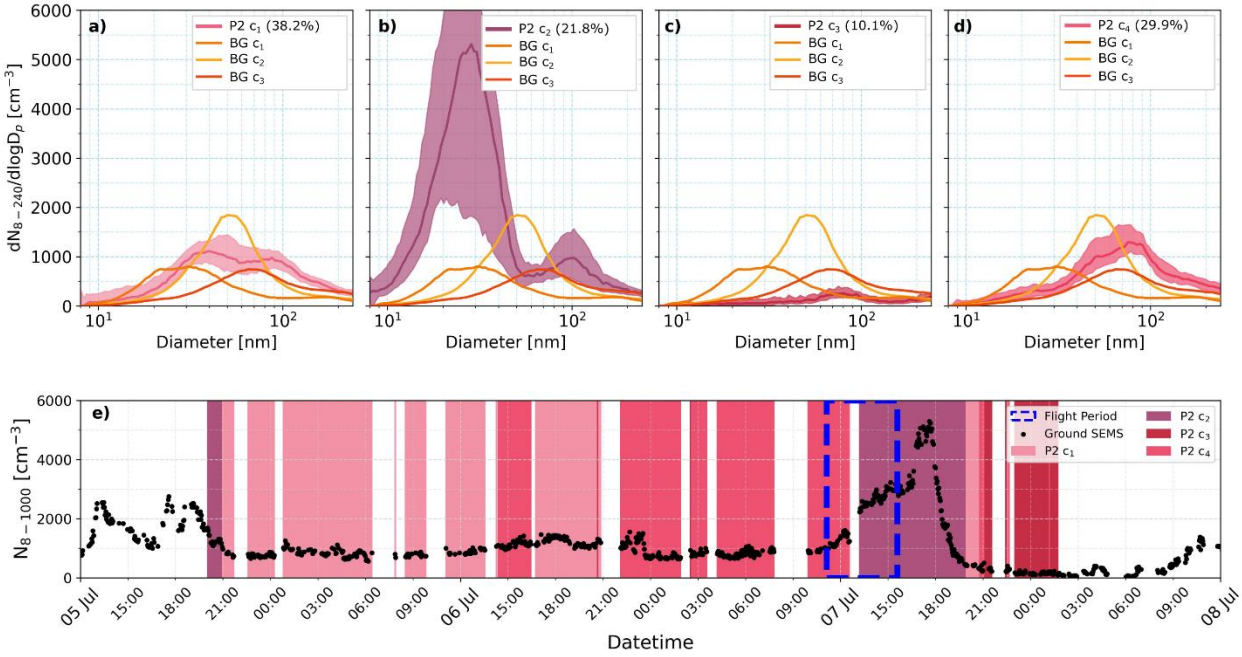


**Figure S14 :** Panels a) to d) show clustered PNSD (light and dark pink, purple, red) covering the time period of *plume 2* compared to the clean *background* clusters (yellow, orange and red). Median values and IQR are shown for each clustered PNSD. Legends show the percentage of scans per cluster. Panel e) shows total number concentration between 8 -1000 nm ($N_{8\text{-}1000}$, black scatter) with the occurrence of each cluster shaded. The time period corresponding to the helikite flight are boxed in blue dashes.

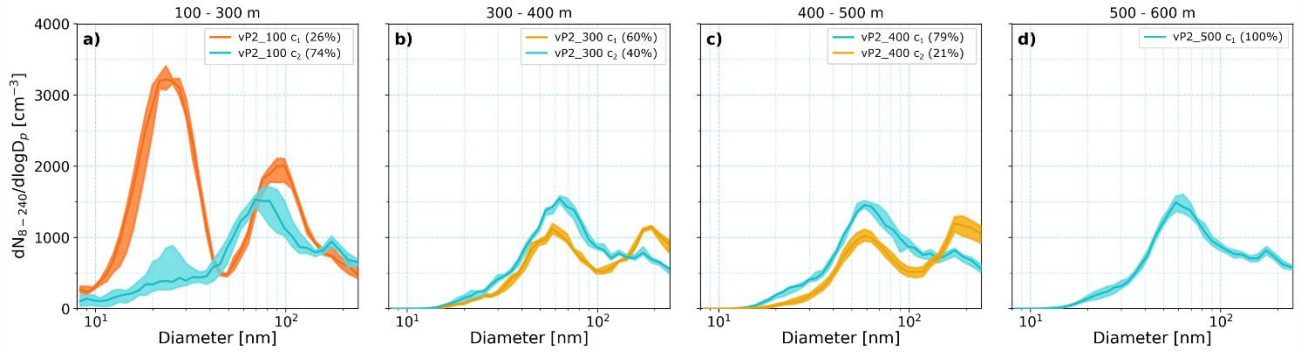


**Figure S15:** Clustered PNSDs using mSEMS vertical measurements taken during a flight on the 7th July for altitude bins of a) 100 to 300 m, b) 300 to 400 m, c) 400 to 500 m and, d) 500 to 600 m above ground level. Median values and IQR are shown for each clustered PNSD. Legends show the percentage of scans per cluster.

To assess how *plume 2* influenced the aerosol profile above the surface, vertical clustering was applied to mSEMS measurements collected during a flight on 7 July (11:02–15:35 LT)**.** Figure S15a-b shows clustered PNSDs for this flight divided into altitude bins of 100–300 m, 300–400 m, 400–500 m, and 500–600 m. Unlike with *plume 1*, the helikite did not directly enter the plume. Instead, we captured the evolution of the aerosol population across multiple vertical layers below the plume. At every altitude, a bi-modal cluster was found, with a dominant Aitken mode between 58 – 69 nm (blue PNSDs in Fig. S15**Error! Reference source not found.**) and an accumulation mode peaking at ~170 nm. Notably, these vertical clusters had elevated particle concentrations between 100 and 240 nm compared to ground-level clusters, consistent with aged plume signatures. This bi-modal cluster (*vP2_100 c2*) in the lowest altitude range also shows evidence of a weak nucleation mode shoulder at ~25 nm. This is due to the flight take off coinciding with the onset of a particle growth event (compare also to cluster P2 $c_2$). On return of the helikite towards the ground, a strong nucleation mode cluster (v*P2_100 c1*) can be seen between 100-300 m showing the progression of this event in the ~ 3 hours since the ascent profile was measured. Two temperature inversions were observed in the profile (Fig. S18), one between ~0-170 m ($\Delta T/\Delta H$ = 1.01 – 1.90 °C / 100 m), and another from above 500 m ($\Delta T/\Delta H$ = 1.19 °C / 100 m), which likely restricted mixing and confined the nucleation mode to the near-surface layer.

A significant enhancement in the concentration of particles in the accumulation mode between 100 and 240 nm is seen in clusters *vP2_300 c1* and v*P2_400 c1,* with a strong accumulation mode peak at ~175 nm, and a Hoppel minimum at ~100 nm. The large accumulation mode diameter seems to be indicative of the biomass burning plume aerosol based on the observations in plume 1. However, based on the beta attenuation observations by the ceilometer (Fig. 11b), this plume seemed to have remained above helikite reach. Nevertheless, a visible, even though not very optically thick, downward branching of the plume can be seen well before the start of the flight on 6 July. This suggests that while the ceilometer cannot discern the plume at lower elevations, still downmixing of plume aerosol occurred as our helikite observations corroborate. Contrary to plume 1, the impact on the ground aerosol population is however small.

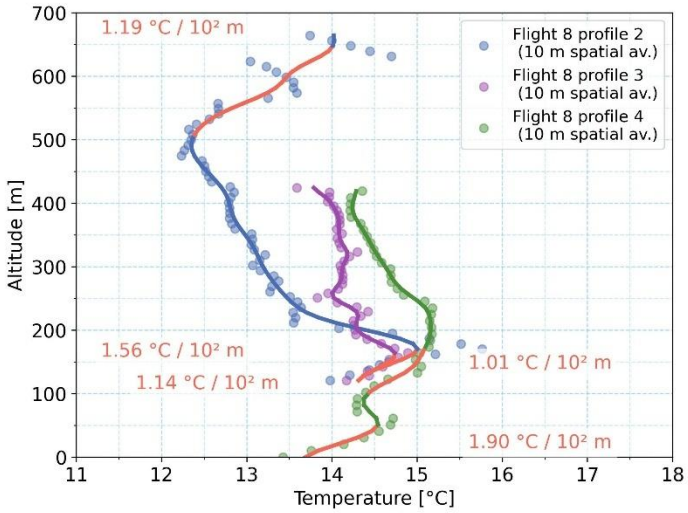


**Figure S16:** Temperature profiles taken using the helikite between 11:02-15:35LT on the 7th July,2023. Temperature inversions are indicated in orange.

## S8. Plume 3

Plume 3 was potentially the most aged plume. Figure S17a-c shows the clustered PNSDs for the period from the ground measurements. Three clusters were found to describe this plume on the ground: 1) a first broadened bi-modal cluster peaking at 57 nm (*P3 $c_1$*) and again above 240 nm (out of measurement range); 2) a second bi-modal cluster peaking just above the nucleation mode region at 29 nm and in the Aitken mode at 93 nm (*P3 $c_2$*); and 3) a third bi-modal cluster peaking in the nucleation mode at 20 nm and in the Aitken mode at 69 nm (*P3 $c_3$*). *P3 $c_3$* occurs most frequently, representing 39.8 % of the time during this plume period. All 3 clusters have a vastly broadened Aitken mode reaching well into the accumulation mode, with *P3 $c_2$* and *P3 $c_3$* showing growth of the nucleation mode from 20 to 29 nm. Compared to the previous 2 plume periods, the concentration of aerosols across the size distribution is visibly lower, more comparable with *background* concentrations.

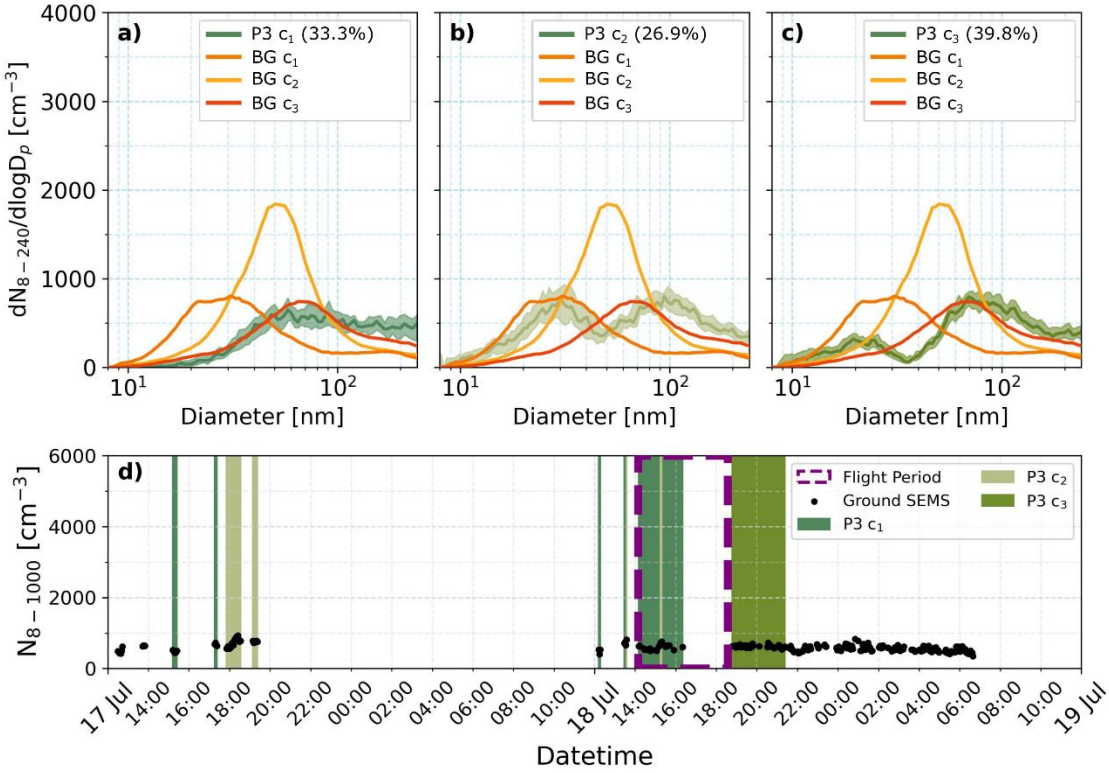


**Figure S17:** Panels a) to c) show clustered PNSD (green) covering the time period of *plume 3* compared to the clean *background* clusters (yellow, orange and red). Median values and IQR are shown for each clustered PNSD. Legends show the percentage of scans for each cluster. Panel d) shows the time series of total number concentration between 8 -1000 nm ($N_{8\text{-}1000}$, black scatter) with the occurrence of each cluster shaded. Time periods corresponding to helikite flights are boxed in purple dashes. Gaps in the $N_{8\text{-}1000}$ data were due to SEMS being switched off overnight.

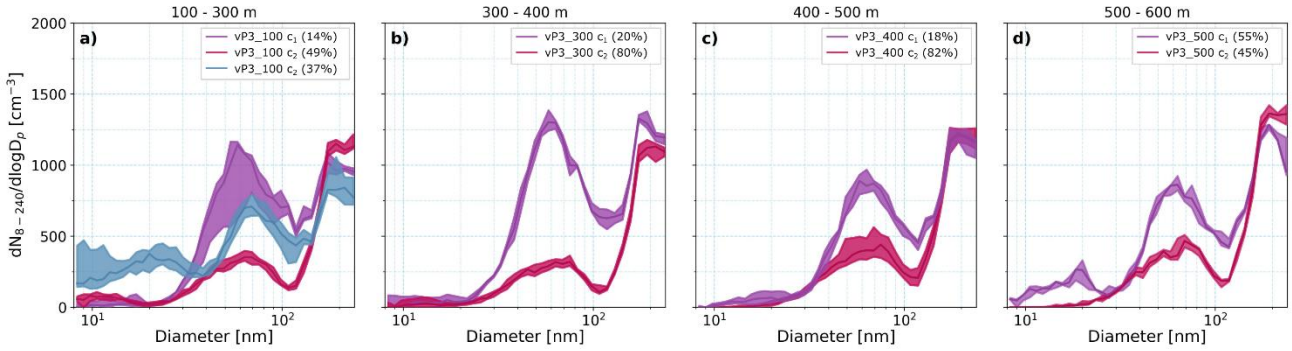


**Figure S18:** Clustered PNSDs using mSEMS vertical measurements for altitude bins of a) 100 to 300 m, b) 300 to 400 m, c) 400 to 500 m and, d) 500 to 600 m above ground level. Median values and IQR are shown for each clustered PNSD. Legends show the percentage of scans per cluster**.**

Figure S18 shows clustered PNSDs from vertical measurements taken during the flight on 18th July (14:09 – 18:34). Three clusters were found to describe the vertical structure with respect to the aerosol population between 100-300 m: 1) a bi-modal cluster peaking in the Aitken and accumulation modes at 58 and 170 nm (v*P3_100 c1*); a second bi-modal cluster peaking broadly between 65 – 75 nm in the Aitken mode and >170 nm (v*P3_100 c2*); and a tri-modal cluster peaking in the nucleation mode at 20 nm, in the Aitken mode at 69 nm and >210 nm in the accumulation mode (v*P3_100 c3*). A nucleation mode cluster matching *vP3_100 c3* was also observed in ground-level PNSDs shortly after the flight, with identical mode diameters**,** suggesting that the lower 300 m of the atmosphere were well-mixed. This is despite the presence of an inversion, which extended to the maximum altitude of the flight at the beginning of the afternoon, then dissolved and later formed again between the surface and 150 m (Fig. S19). Above 300 m, in all altitude ranges, similar cluster structures reappear with minimal change in mode diameters, indicating a more homogeneous aerosol population. The absence of a nucleation mode cluster in the 300-500 m altitude range is likely due to the temperature inversion. The strong accumulation mode signal persists up to 600 m, showing that aerosol layers above the inversion are influenced mainly by regional transport and less by nucleation in the surface layer. However, above 500 m an aged nucleation mode is again visible in v*P3_500 c1*, but it does not influence the aerosol layer beneath likely due to the temperature inversion, showcasing another case of dual-layer nucleation signatures separated by thermal stratification.

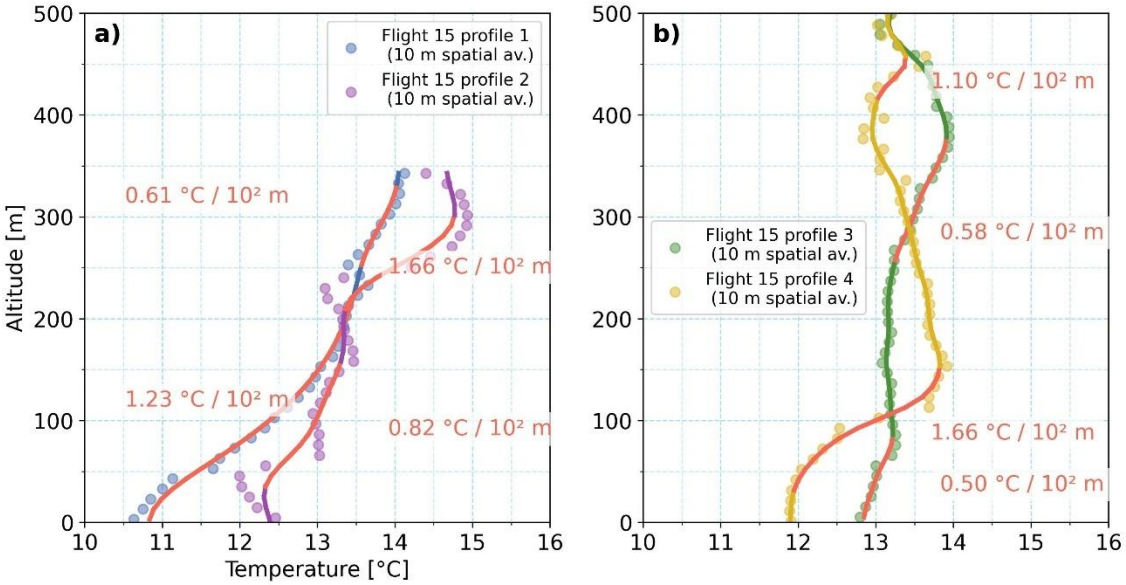


**Figure S19:** Temperature profiles taken using the helikite between 14:09-18:34LT on the 18th July,2023. Temperature inversions are indicated in orange.

285

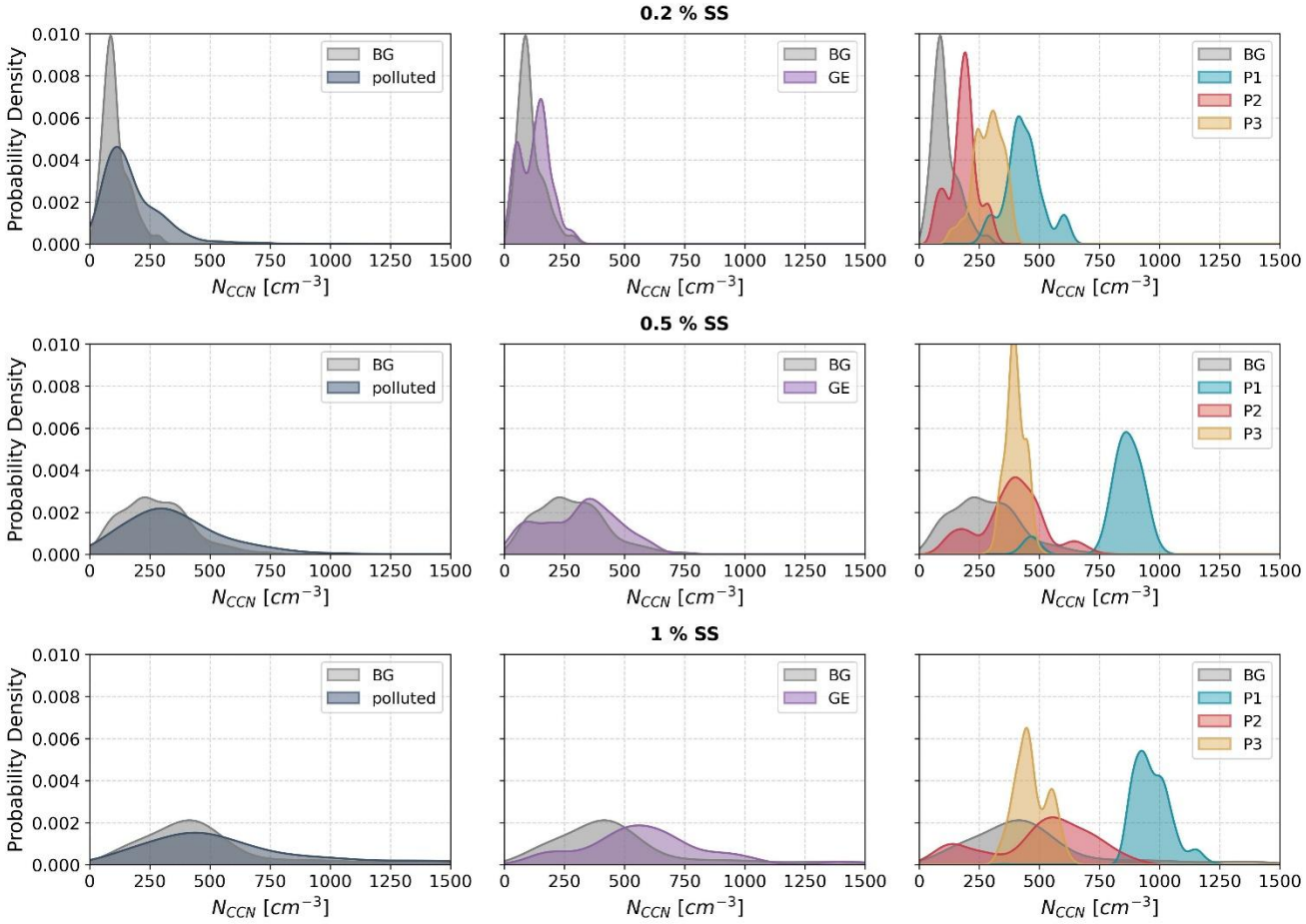


**Figure S20.** Probability density plot of a-c) $N_{CCN}$ at 0.2 % supersaturation, d-f) $N_{CCN}$ at 0.5 % and g-f) $N_{CCN}$ at 1 % for polluted (navy), growth event (purple), plume 1(blue), plume 2 (crimson) and plume 3 (yellow) conditions relative to BG (grey) conditions.

290

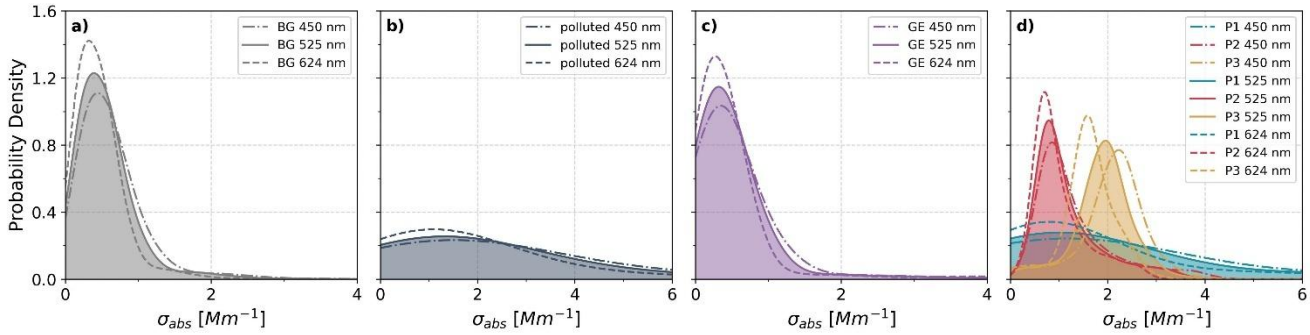


**Figure S21.** Comparison of probability density distribution of $\sigma_{abs}$ at wavelengths 450, 525 and 624 nm for polluted (navy), GE (purple), plume 1(blue), plume 2 (crimson) and plume 3 (yellow) conditions relative to BG (grey) conditions.

Plumes 1 and 2 exhibit similar absorption characteristics in terms of mode and wavelength dependence, although plume 2 displays more pronounced tails. In contrast, plume 3 shows stronger overall absorption, with a marked increase at shorter wavelengths. This pattern may suggest a greater contribution from light-absorbing organic aerosols, potentially originating from different fuel types and fire conditions, such as increased smouldering or peat combustion, compared to the other plumes.

**References**


Ansmann, A., Tesche, M., Groß, S., Freudenthaler, V., Seifert, P., Hiebsch, A., Schmidt, J., Wandinger, U., Mattis, I., Müller, D., and Wiegner, M.: The 16 April 2010 major volcanic ash plume over central Europe: EARLINET lidar and AERONET photometer observations at Leipzig and Munich, Germany, Geophysical Research Letters, 37, 2010GL043809, https://doi.org/10.1029/2010GL043809, 2010.

Burton, S. P., Hair, J. W., Kahnert, M., Ferrare, R. A., Hostetler, C. A., Cook, A. L., Harper, D. B., Berkoff, T. A., Seaman, S. T., Collins, J. E., Fenn, M. A., and Rogers, R. R.: Observations of the spectral dependence of linear particle depolarization ratio of aerosols using NASA Langley airborne High Spectral Resolution Lidar, Atmos. Chem. Phys., 15, 13453–13473, https://doi.org/10.5194/acp-15-13453-2015, 2015.

Fochesatto, G. J.: Methodology for determining multilayered temperature inversions, Atmos. Meas. Tech., 8, 2051–2060, https://doi.org/10.5194/amt-8-2051-2015, 2015.

Groß, S., Freudenthaler, V., Wiegner, M., Gasteiger, J., Geiß, A., and Schnell, F.: Dual-wavelength linear depolarization ratio of volcanic aerosols: Lidar measurements of the Eyjafjallajökull plume over Maisach, Germany, Atmospheric Environment, 48, 85–96, https://doi.org/10.1016/j.atmosenv.2011.06.017, 2012.

Groß, S., Esselborn, M., Weinzierl, B., Wirth, M., Fix, A., and Petzold, A.: Aerosol classification by airborne high spectral resolution lidar observations, Atmos. Chem. Phys., 13, 2487–2505, https://doi.org/10.5194/acp-13-2487-2013, 2013.

Haarig, M., Ansmann, A., Baars, H., Jimenez, C., Veselovskii, I., Engelmann, R., and Althausen, D.: Depolarization and lidar ratios at 355, 532, and 1064 nm and microphysical properties of aged tropospheric and stratospheric Canadian wildfire smoke, Atmos. Chem. Phys., 18, 11847–11861, https://doi.org/10.5194/acp-18-11847-2018, 2018.

Kulmala, M., Petäjä, T., Nieminen, T., Sipilä, M., Manninen, H. E., Lehtipalo, K., Dal Maso, M., Aalto, P. P., Junninen, H., and Paasonen, P.: Measurement of the nucleation of atmospheric aerosol particles, Nature protocols, 7, 1651–1667, 2012.

Lehtinen, K. E. J., Dal Maso, M., Kulmala, M., and Kerminen, V.-M.: Estimating nucleation rates from apparent particle formation rates and vice versa: Revised formulation of the Kerminen–Kulmala equation, Journal of Aerosol Science, 38, 988–994, https://doi.org/10.1016/j.jaerosci.2007.06.009, 2007.

Mayfield, J. A. and Fochesatto, G. J.: The Layered Structure of the Winter Atmospheric Boundary Layer in the Interior of Alaska, Journal of Applied Meteorology and Climatology, 52, 953–973, https://doi.org/10.1175/JAMC-D-12-01.1, 2013.

Pohorsky, R., Baccarini, A., Brett, N., Barret, B., Bekki, S., Pappaccogli, G., Dieudonné, E., Temime-Roussel, B., D'Anna, B., Cesler-Maloney, M., Donateo, A., Decesari, S., Law, K. S., Simpson, W. R., Fochesatto, J., Arnold, S. R., and Schmale, J.: In situ vertical observations of the layered structure of air pollution in a continental high-latitude urban boundary layer during winter, Atmos. Chem. Phys., 25, 3687–3715, https://doi.org/10.5194/acp-25-3687-2025, 2025.

Soldati, G. A.: Ceilometer data processing and analysis, 2024.

Thinsungnoen, T., Kaoungku, N., Durongdumronchai, P., Kerdprasop, K., and Kerdprasop, N.: The Clustering Validity with Silhouette and Sum of Squared Errors, in: The Proceedings of the 2nd International Conference on Industrial Application

Engineering 2015, International Conference on Industrial Application Engineering 2015, 44–51, https://doi.org/10.12792/iciae2015.012, 2015.